

LA-UR-19-31432 (Accepted Manuscript)

Deformation mechanisms and ductile fracture characteristics of a friction stir processed transformative high entropy alloy

Sinha, S
Nene, S.S.
Frank, M.
Liu, K.
Lebensohn, Ricardo A.
Mishra, R.

Provided by the author(s) and the Los Alamos National Laboratory (2020-12-04).

To be published in: Acta Materialia

DOI to publisher's version: 10.1016/j.actamat.2019.11.056

Permalink to record: <http://permalink.lanl.gov/object/view?what=info:lanl-repo/lareport/LA-UR-19-31432>

Disclaimer:

Los Alamos National Laboratory, an affirmative action/equal opportunity employer, is operated by Triad National Security, LLC for the National Nuclear Security Administration of U.S. Department of Energy under contract 89233218CNA000001. By approving this article, the publisher recognizes that the U.S. Government retains nonexclusive, royalty-free license to publish or reproduce the published form of this contribution, or to allow others to do so, for U.S. Government purposes. Los Alamos National Laboratory requests that the publisher identify this article as work performed under the auspices of the U.S. Department of Energy. Los Alamos National Laboratory strongly supports academic freedom and a researcher's right to publish; as an institution, however, the Laboratory does not endorse the viewpoint of a publication or guarantee its technical correctness.

Deformation mechanisms and ductile fracture characteristics of a friction stir processed transformative high entropy alloy

S. Sinha¹, S.S. Nene¹, M. Frank¹, K. Liu¹, R.A. Lebensohn², R.S. Mishra^{1*}

¹Department of Materials Science and Engineering, Center for Friction Stir Processing, Advanced Materials Manufacturing Processes Institute, University of North Texas, Denton, TX 76207 USA

²Theoretical Division, Los Alamos National Laboratory, Los Alamos, NM 87544 USA

*Corresponding author email: Rajiv.Mishra@unt.edu

Abstract

Deformation mechanisms of a friction stir processed Fe₄₀Mn₂₀Co₂₀Cr₁₅Si₅ transformative high entropy alloy using three different process parameters were studied to explain the microstructural dependence of tensile response in these specimens. The relative strain hardening contribution due to transformation and twinning effects was different for the three different microstructural conditions and thus resulted in different magnitude of work hardening. Crystal plasticity simulations confirmed that synergistic activity of face centered cubic and hexagonal close packed slip and twin mechanisms resulted in sustained work hardening and enhanced uniform elongation. The non-uniform ductility and extent of void nucleation and growth in these specimens were limited. Nevertheless, fractography and X-ray microscopy of fractured tensile specimens verified that microstructural flexibility induced different propensities for void growth and ductile fracture mode. Thus, alloy design induced phase stability, adaptive phase evolution due to friction stir processing, extent and kinetics of martensitic transformation and related work hardening capability of the individual phases combined together to determine the overall tensile response. The crystallographic orientation dependence of deformation induced phase transformation was also thoroughly studied. This study included quantitative determination of the crystallographic orientation where resolved shear stress on leading and trailing partial dislocations favored separation of the partials to cause transformation at a critical value of applied stress.

Keywords

Martensitic transformation; Tensile behavior; Ductile fracture; Crystal plasticity; Partial dislocation separation

1. Introduction

Extensive research in recent years established that during tensile deformation, high entropy alloys with transformation induced plasticity (TRIP-HEAs) show exceptional work hardening behavior, which thus accounts for superior strength-ductility combination [1–5]. These previous studies proved that the enhanced tensile properties can be attributed to the activation of multiple plastic deformation mechanisms. Our earlier studies discussed the tensile behavior of various transformative HEAs, wherein microstructural tailoring through alloy design and thermomechanical processing resulted in enhanced tensile strength-ductility response [6–8]. The TRIP effect in our HEAs is based on face centered cubic (f.c.c.) γ to hexagonal close packed (h.c.p.) ϵ -martensite phase transformation [1–2], although other studies have also discussed TRIP-HEAs involving body centered cubic (b.c.c.) to h.c.p./orthorhombic martensitic transformation [9–10].

This study was a systematic investigation to compare and contrast the deformation mechanisms that ultimately result in different degrees of work hardenability for a particular TRIP-HEA. In order to perform a systematic study, we selected a specific transformative HEA with processing-dependent microstructural flexibility. One of our earlier studies discussed $\text{Fe}_{40}\text{Mn}_{20}\text{Co}_{20}\text{Cr}_{15}\text{Si}_5$ alloy (CS-HEA), processed by friction stir processing (FSP) using different tool rotation rates [6]. FSP with different tool rotation rates (S350, S150 and D-pass, described in Table 1) led to different phase evolution. Subsequently, these specimens exhibited different tensile response, which was reported in our earlier study [6]. Our aim in the present study was to compare quantitatively the work hardening behavior of the three different microstructural conditions of CS-HEA (responsible for their respective uniform ductility).

Additionally, studies on fracture behavior of TRIP-HEAs are limited. Recently, Wei et al. investigated the fracture mechanisms in a metastable $\text{Fe}_{45}\text{Mn}_{35}\text{Co}_{10}\text{Cr}_{10}$ HEA [11]. Still, the scope for investigating the fracture mechanisms of TRIP-HEAs is wide. Key to our inquiries is the realization that although transformative HEAs exhibit large uniform ductility due to sustained work hardening response, their non-uniform ductility is quite limited. Such non-uniform ductility represents strain for growth of voids and ductile fracture. Clearly, the ductile failure mechanisms must be distinguished from the deformation mechanisms that contribute to work hardening in the uniform elongation regime. In line with this, Luo and Huang discussed three different types of ductile fracture surfaces: (i) quasi-cleavage (ii) void sheet and (iii) large dimples [12].

Ductile failure can occur by two generic modes, namely plastic instability and void coalescence. Different materials exhibit different mechanisms of ductile fracture by void

nucleation/growth in the absence or presence of necking. Twinning induced plasticity (TWIP) steels undergo failure by localized plastic shear without necking; 304 stainless steel fails by localized plastic shear after necking, while Interstitial Free (IF) steel shows failure by void coalescence with obvious necking [12]. The strain for nucleation and growth of voids has been described based on Considère criterion for plastic instability. Several researchers proposed ductile fracture criteria based on the original or modified Brown and Embury model [13–16] to describe the nucleation and growth of voids. Investigation of void nucleation and growth characteristics is important in elaborating the ductile failure behavior of transformative HEAs.

Therefore, we performed a detailed investigation of the ductile fracture mechanisms of CS-HEA using fractography and X-ray microscopy (XRM). This study seeks to provide a comprehensive overview of the factors contributing to large uniform ductility as well as the reasons for low non-uniform ductility and mode of failure.

2. Experimental

The material used in the present investigation was $\text{Fe}_{40}\text{Mn}_{20}\text{Co}_{20}\text{Cr}_{15}\text{Si}_5$ HEA (CS-HEA). The alloy was produced by vacuum arc-casting in a cold copper crucible using pure metals and ingot dimensions of $300 \times 100 \times 6 \text{ mm}^3$. The chamber was backfilled with argon to 1 atm. prior to each melt.

FSP of as-cast CS-HEA sheets was performed using a W-Re tool with shoulder diameter of 12 mm with tapered pin and root diameter, pin diameter and tool length of 7.5 mm, 6 mm and 3.5 mm, respectively. The FSP parameters are listed in Table 1.

Table 1: FSP parameters used in the present study

Condition	Pass	Rotational rate (rpm)	Traverse speed (mm/min.)	Plunge Depth (mm)	Tilt Angle (°)
S350	Single	350	50.8	3.65	2.0
S150	Single	150	50.8	3.65	2.0
D-pass	Pass 1	350	50.8	3.65	2.0
	Pass 2	150	50.8	3.70	2.0

Rectangular dog-bone shaped mini-tensile specimens with gage length, gage width and thickness of 5 mm, 1.25 mm and 1 mm, respectively, were machined out using a mini computer numerical control (CNC) machine from 1 mm below the surface within the nugget region of the FSP specimens. Room-temperature tensile tests to failure were performed on a mini-tensile tester

using an initial strain rate of 10^{-3} s^{-1} . To check the reproducibility of results, three tests were carried out for each condition.

Electron backscatter diffraction (EBSD) characterization of microstructure was done on a FEI Nova Nano SEM 230 equipped with Hikari Super EBSD detector at an operating voltage of 20 kV. TEAM™ software for EBSD data acquisition and TSL OIM 8 software for EBSD data analysis were used. The EBSD scans of FSP specimens were done at higher magnification than the as-cast condition due to finer grain size in the former. The typical scan area and step size of the EBSD scans for as-cast material were $150 \mu\text{m} \times 120 \mu\text{m}$ and $0.5 \mu\text{m}$, respectively. The corresponding values for the FSP specimens were $39 \mu\text{m} \times 20 \mu\text{m}$ and $0.1 \mu\text{m}$, respectively. Phase fractions reported from EBSD were obtained by averaging three or more scans. Fractography of the fractured tensile specimens were performed using FEI Nova Nano SEM 230 and FEI Quanta 200 ESEM.

X-ray microscopy (XRM) of fractured mini-tensile specimens of CS-HEA was accomplished using a Zeiss Xradia Versa 520 microscope. For each specimen condition, a full field-of-view scan at lower magnification (4X objective) and an interior tomography at higher magnification (20X objective) were carried out to image the fractured half-tensile specimen and detailed fracture surface, respectively. The parameters used for the XRM scans are detailed in Table 2. Voltage and power, exposure time and source to detector distances were optimized depending on the objective, so as to obtain intensity of at least 5000 counts per second. In each case, the filter was selected by checking the transmittance at the angular position of 45° . First, the transmittance with air filter was recorded. Based on that transmittance, the appropriate filter was then selected to increase transmittance in the range of 20–35%. XRM data analysis was carried out using Dragonfly software.

Table 2: XRM parameters used to study fracture behavior of CS-HEA

Specimen	S350		D-pass		S150	
	Objective	Objective	Objective	Objective	Objective	Objective
Objective	4X	20X	4X	20X	4X	20X
Voltage (kV)	80	80	120	120	120	100
Power (W)	7	7	10	10	10	9
Filter	LE5	LE6	LE5	HE3	HE1	LE6
Binning	2	4	2	4	2	4
Exposure(s)	5	10	1	10	1	10
Source Position (mm)	-30.07	-14.55	-30.60	-16.39	-30.05	-14.57
Detector Position (mm)	30.07	21.75	30.61	25.25	30.05	21.75
Angular range (°)	360	360	360	360	360	360
Number of Projections	1601	3601	1601	3601	1601	3601

3. Computational

3.1. Theoretical calculation of dislocation and geometrical hardening

The experimental stress-strain responses for S350, D-pass and S150 specimens were compared with calculated hardening contributions based on dislocation hardening [17-21] and geometrical hardening [22-23]. The original Taylor equation for dislocation hardening is given as,

$$\tau = \tau_0 + \alpha Gb\sqrt{\rho} \quad (1)$$

where τ is shear flow stress, τ_0 is shear resistance to dislocation motion when $\rho \approx 0$, α is a dimensionless material parameter, G is shear modulus and ρ is dislocation density. Also, the relationship between shear flow stress τ and uniaxial flow stress σ of a polycrystal is $\sigma = M\tau$ where M is the Taylor factor. Using these, the Taylor equation can be expressed in the alternate form as,

$$\sigma = \sigma^* + M\alpha Gb(\sqrt{\rho} - \sqrt{\rho^*}) \quad (2)$$

where σ^* and ρ^* are flow stress and dislocation density at the point where the material first becomes plastic. Differentiating Eq. (2) to get the stress evolution with dislocation density yields

$$d\sigma/d\rho = M\alpha Gb/2\sqrt{\rho}. \quad (3)$$

A linear Taylor dislocation hardening can be obtained by considering a constant slope $(d\sigma/d\rho)_{\text{const}}$. An initial estimate of $\rho_{\text{const}} = 10^{12}/\text{m}^2$ was used to calculate the $(d\sigma/d\rho)_{\text{const}}$. The values of $M = 3.1$, $\alpha = 1.16$ [24], $G = 78$ GPa ($G = E/(2(1+\nu))$ where $E =$ Young's modulus = 205 GPa and $\nu =$ Poisson ratio = 0.3) and $b = 4.3321$ Å (corresponding to $\langle c+a \rangle$ system) were applied to calculate $(d\sigma/d\rho)_{\text{const}}$. Then the experimental values of stress σ and $(d\sigma/d\rho)_{\text{const}}$ were used to obtain values of ρ (dislocation evolution according to a linear Taylor hardening model). Finally, the stress σ according to a linear Taylor hardening model (that is, the $M\alpha Gb\sqrt{\rho}$ contribution as described by Eq. (2)) was calculated using the calculated values of ρ . The value of ρ_{const} used to calculate $(d\sigma/d\rho)_{\text{const}}$ was refined by iteration until the $M\alpha Gb\sqrt{\rho^*}$ was equal to experimental σ^* (at the yield stress) up to 3 decimal places.

Similarly, the geometric hardening contribution due to crystal lattice rotation with strain was calculated by applying the equation for glide shear strain τ given as [25],

$$\tau = (P/A)\sin\chi_0[1 - \{\sin^2\lambda_0/(L_i/L_0)\}]^{1/2} \quad (4)$$

where P and A are the applied load and area that specify the applied stress, χ_0 and λ_0 are the angles specifying the initial orientations of the slip plane and slip direction with respect to the tensile (loading) axis, L_i and L_0 are the instantaneous and original gage lengths, respectively;

1
2
3
4 hence, L_i/L_0 represents the engineering strain. A range of values of χ_0 and λ_0 based on a
5 theoretical range of possible Schmid factors (e.g., from 0.01 to 0.45) enabled calculating the
6 theoretical geometric hardening contribution.
7
8

9 10 11 **3.2. Visco-plastic self-consistent (VPSC) simulations**

12 The VPSC model simulates the plastic deformation of polycrystalline aggregates based on
13 physical shear mechanisms of slip and twinning and accounts for grain interaction effects [26-
14 27]. Each grain is considered as an ellipsoidal inclusion in a homogeneous medium, where both
15 the inclusion and medium properties are anisotropic. VPSC predicts the macroscopic stress-strain
16 response, thereby accounting for hardening, reorientation and shape change of individual grains
17 to predict the hardening and textural evolution of the material with plastic deformation.
18
19

20 Deformation occurs by slip or twinning when the resolved shear stress reaches a critical
21 value. The extended Voce law [28] given by Eq. (5) describes the evolution of critical stress with
22 deformation,
23

$$24 \hat{\tau}^s = \tau_0^s + (\tau_1^s + \theta_1^s \Gamma)(1 - \exp(-\Gamma|\theta_0^s/\tau_1^s|)) \quad (5)$$

25 where $\Gamma = \sum_s \Delta\gamma^s$ is the accumulated shear in the grain, and τ_0 , θ_0 , θ_1 , $(\tau_0+\tau_1)$ are the initial
26 critical resolved shear stress (CRSS), initial hardening rate, asymptotic hardening rate and back-
27 extrapolated CRSS, respectively. Additionally, self and latent hardening are allowed by defining
28 coupling coefficients (h^*) to account for the interactions between slip/twin systems.
29

30 In the present study, VPSC simulations of uniaxial tensile deformation of S350, S150 and
31 D-pass conditions of CS-HEA were performed to obtain insight into the relative propensities of
32 slip and twin modes, to explain the differences in work hardening behavior. The initial textures
33 (in the form of Euler angles ($\varphi_1, \phi, \varphi_2$)) of as-FSP condition of S350, S150 and D-pass specimens
34 obtained from EBSD were used as input for the VPSC simulations. Phase fractions of γ (f.c.c.)
35 and ε (h.c.p.) derived from EBSD were also specified as input (S350: 5% γ + 95% ε , S150: 65%
36 γ + 35% ε , D-pass: 31% γ + 69% ε). To obtain appropriate Voce parameters (τ_0 , τ_1 , θ_0 , θ_1) to
37 model the hardening behavior, initially we started with hardening parameters reported for TWIP
38 steels for the γ (f.c.c.) phase [29] and conventional h.c.p. metals like Mg/Ti for the ε (h.c.p.)
39 phase [30-33]. The Voce parameters were changed and refined by comparing the simulated
40 stress-strain response for each specimen condition with the corresponding experimental curves
41 (with every new set of (τ_0 , τ_1 , θ_0 , θ_1)). This refinement was repeated until a reasonably good
42 match was obtained between experimental and simulated curves for each specimen condition
43 (S350, S150 and D-pass). Then, VPSC simulations were performed for all three conditions using
44
45
46
47
48
49
50
51
52
53
54
55
56
57
58
59
60
61
62
63
64
65

the Voce and latent (h^*) hardening parameters listed in Table 3. Note that the γ (f.c.c.) phase is assumed to be softer than the ε (h.c.p.) phase (Table 3) because previous researchers showed through first-principles calculations [34] and experimental micro-hardness measurements [35] that the f.c.c. phase is softer than the h.c.p. phase in HEAs.

Table 3: Voce and latent hardening parameters used in the present study

Specimen	Mode	τ_0 (MPa)	τ_1 (MPa)	θ_0 (MPa)	θ_1 (MPa)	$h^{*,1}$	$h^{*,2}$	$h^{*,3}$	$h^{*,4}$	$h^{*,5}$	$h^{*,6}$
S350	1	275	200	300	50	1	1.4	-	-	-	-
	2	370	200	300	100	1	1.4	-	-	-	-
	3	470	40	340	60	-	-	1	1	10	2
	4	490	50	390	80	-	-	1	1	10	2
	5	540	60	1200	40	-	-	1	1	2	2
	6	530	60	1000	20	-	-	1	1	10	16
S150	1	275	200	300	50	1	1.4	-	-	-	-
	2	370	200	300	100	1	1.4	-	-	-	-
	3	730	100	900	80	-	-	1	1	10	2
	4	750	110	1000	100	-	-	1	1	10	2
	5	800	50	2500	40	-	-	1	1	2	2
	6	790	50	2000	60	-	-	1	1	10	16
D-pass	1	275	200	300	50	1	1.4	-	-	-	-
	2	370	200	300	100	1	1.4	-	-	-	-
	3	450	60	330	100	-	-	1	1	10	2
	4	470	70	380	120	-	-	1	1	10	2
	5	520	80	1200	80	-	-	1	1	2	2
	6	510	80	1000	60	-	-	1	1	10	16
Description of modes						Initial grain shape (initial ellipsoid ratios)					
1: FCC $\{111\}$ $\langle 1\bar{1}0 \rangle$ Slip						S350: 5:1:1 for fcc and 1:1:1 for hcp					
2: FCC $\{111\}$ $\langle 11\bar{2} \rangle$ Twin						S150 and D-pass: 1:1:1 for both fcc and hcp					
3: HCP $\{10\bar{1}0\}$ $\langle 11\bar{2}0 \rangle$ Prismatic Slip						Phase fractions					
4: HCP $\{0001\}$ $\langle 11\bar{2}0 \rangle$ Basal Slip						S350: 5% fcc + 95% hcp					
5: HCP $\{10\bar{1}1\}$ $\langle 11\bar{2}3 \rangle$ Pyramidal $\langle c+a \rangle$ Slip						S150: 65% fcc + 35% hcp					
6: HCP $\{10\bar{1}2\}$ $\langle 10\bar{1}1 \rangle$ Extension Twin						D-pass: 31% fcc + 69% hcp					

4. Results

4.1. Uniform ductility and work hardening mechanisms

CS-HEA has ε (h.c.p.) dominant dual-phase microstructure in the as-cast condition (Fig. 1 (a)). The phase evolution in as-FSP specimens is different for the different FSP parameters (S350, S150 and D-pass), and results in three different microstructures (Fig. 1 (a)). S350 yields almost single-phase ε (h.c.p.) microstructure, S150 has γ (f.c.c.) dominant dual-phase microstructure, while D-pass specimen displays ε (h.c.p.) dominant dual-phase microstructure.

1
2
3
4 The corresponding tensile and strain hardening curves are included in Figs. 1 (b) and (c),
5 respectively. Note that the comparison of the tensile response of as-FSP specimens with that of
6 as-cast specimen was discussed in our earlier study [6]. Among the as-FSP specimens, D-pass
7 condition exhibits the highest tensile elongation, while S150 shows the lowest ductility. The
8 higher elongation to failure of D-pass specimen is attributed to higher, sustained strain hardening
9 due to TRIP and twinning [6].
10

11 Figure 1 (d) presents a comparison of the ϵ (h.c.p.) fraction change from as-FSP to deformed
12 condition for the three processing conditions (S350, S150 and D-pass), and the corresponding
13 uniform elongation (which also corresponds to the void nucleation strain related to the onset of
14 plastic instability). Clearly, the uniform elongation is dependent on the interplay between the
15 amounts of ϵ (h.c.p.) already present in the as-FSP microstructure and ϵ (h.c.p.) formed due to
16 transformation, as well as the work hardening characteristics of deformed ϵ (h.c.p.). The fact that
17 the D-pass specimen shows the highest uniform elongation indicates that the γ (f.c.c.) phase
18 stability is an important factor. Conceptually, if the alloy is more metastable, the TRIP stress
19 would be lower and backstresses would not be able to hinder transformation. CS-HEA is highly
20 metastable due to alloy design. Now, considering that S350 has a higher ϵ/γ ratio than the D-pass
21 in the as-FSP condition (Fig. 1 (d)), we can infer that pronounced TRIP effect in D-pass
22 condition contributes to highest work hardening and uniform ductility. Also, the high work
23 hardening in D-pass condition is due to the ductile nature of the ϵ (h.c.p.) phase itself. S150
24 condition has γ (f.c.c.) dominant microstructure in the as-FSP condition, and exhibits significant
25 ϵ (h.c.p.) phase formation during deformation (value for the ratio of ϵ increase during
26 deformation and ϵ in as-FSP as shown in Fig. 1 (d)). Yet, S150 shows lowest work hardening
27 and uniform elongation. This is because the kinetics of transformation also influences the
28 deformation capability of the phases. The relative activity of slip modes and amount of twinning
29 of the γ (f.c.c.) and ϵ (h.c.p.) phases are important and will be discussed later from VPSC
30 simulation results. First, we must distinguish among the three specimen conditions based on the
31 extent of work hardening. Even though TRIP/twin effects contribute to work hardening in all
32 three specimen conditions, the degree of work hardening in these specimens is different. Clearly,
33 the relative contribution from TRIP/twin effects is different for each specimen condition. The
34 following discussion seeks to explain the difference in hardening contributions for S350, D-pass
35 and S150 specimens to justify the different extents of work hardening observed.
36
37
38
39
40
41
42
43
44
45
46
47
48
49
50
51
52
53
54
55
56
57
58
59
60
61
62
63
64
65

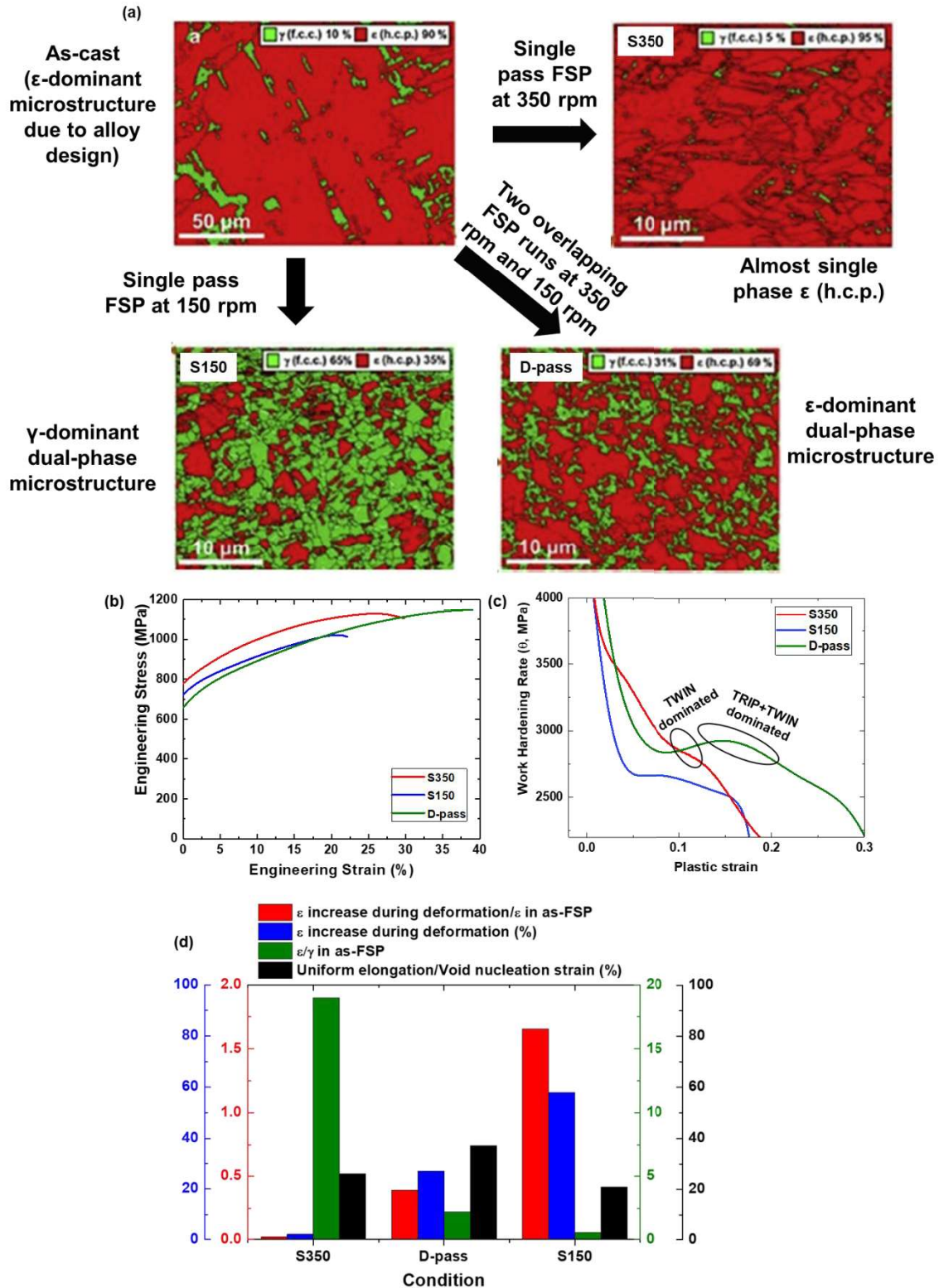


Fig. 1. (a) EBSD phase fraction maps, (b) tensile curves [6], (c) strain hardening curves [6], and (d) comparison of ϵ (h.c.p.) phase fraction change during deformation and uniform elongation of CS-HEA for the various FSP conditions.

1
2
3
4 The predicted curves based on the sum of linear Taylor dislocation hardening and
5 geometrical hardening are plotted along with the experimental curves for S350, S150 and D-pass
6 conditions in Figs. 2 (a), (b) and (c), respectively. Figure 2 (d) illustrates the common features of
7 Figs. 2 (a)–(c) to explain the difference between experimental and theoretical hardening
8 contributions. Clearly, the small geometrical hardening contribution explains why the predicted
9 curves of dislocation plus geometrical hardening almost overlap with the dislocation hardening
10 line in Figs. 2 (a)–(c). Interestingly, the additional hardening contribution from TRIP/twin effects
11 (corresponding to the region shaded by golden dotted lines in the schematic Fig. 2 (d)) is
12 different for the different specimen conditions in Figs. 2 (a)–(c). The calculated linear Taylor
13 dislocation hardening simply represents what would be the hardening arising solely out of the
14 evolution of dislocation content. Similarly, the geometrical hardening estimates the theoretical
15 hardening possible due to lattice reorientation with strain. On the other hand, the additional work
16 hardening (difference between experimental and calculated curves) arises from strain induced by
17 f.c.c. to h.c.p. transformation, backstress generated in the dual-phase microstructure and load
18 partitioning to the martensite phase, thus accounting for the microstructure and stress-state
19 dependence of the work hardening behavior. Figs. 2 (a)–(c) clearly show that the D-pass
20 specimen exhibits the highest additional hardening contribution from TRIP/twin (~ 500 MPa at
21 the UTS). The corresponding values for S350 and S150 specimens are ~ 300 MPa and ~ 200
22 MPa, respectively. Thus, the relative work hardening contributions from TRIP/twin effects are
23 quantified for the different specimen conditions. The lowest TRIP/twin hardening contribution
24 for S150 specimen is due to the fact that kinetics of TRIP is very fast whereas the S350 deforms
25 completely with different preferential strain accommodation mechanisms. Also, it must be
26 mentioned that the stored dislocation density and grain size of the γ (f.c.c.) phase in S150 and D-
27 pass conditions alter the kinetics of TRIP.
28
29
30
31
32
33
34
35
36
37
38
39
40
41
42
43
44
45
46
47
48
49
50
51
52
53
54
55
56
57
58
59
60
61
62
63
64
65

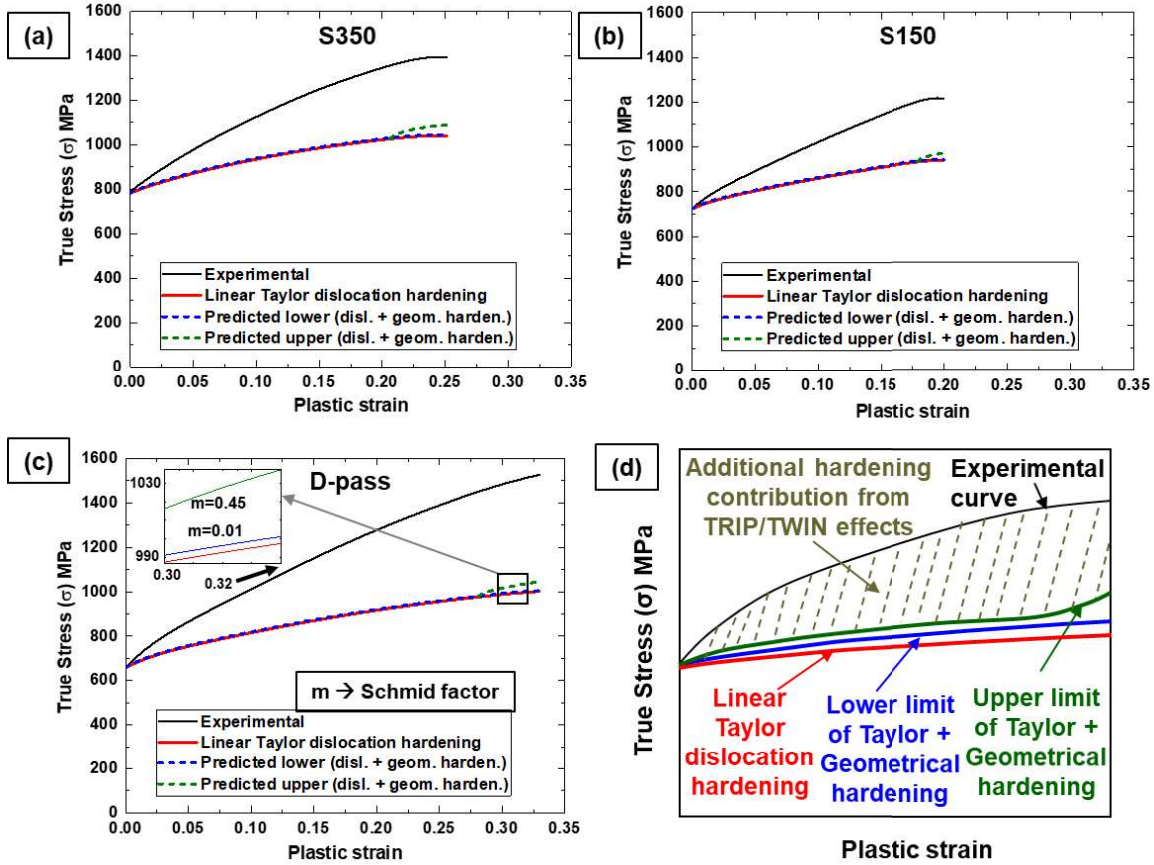


Fig. 2. Calculated hardening contributions in comparison with experimental curves for (a) S350, (b) S150, and (c) D-pass specimens of CS-HEA. (d) A schematic to explain the various hardening contributions and the gap that needs further discussion.

4.2. VPSC simulations of stress-strain response

S350, S150 and D-pass conditions of CS-HEA exhibit different degrees of work hardening due to the synergistic effect of alloy chemistry induced phase stability, adaptive phase evolution due to FSP parameters and propensity and kinetics of γ (f.c.c.) to ϵ (h.c.p.) martensitic transformation. Various factors like phase ratio in the as-FSP state, TRIP stress, rate of phase transformation, stored dislocation content and grain size of γ (f.c.c.) influence the deformability of the γ (f.c.c.) and ϵ (h.c.p.) phases. Therefore, quantifying the relative activity of f.c.c. and h.c.p. deformation mechanisms in each specimen condition is necessary to get a holistic overview of the factors contributing to the different work hardening behaviors.

VPSC simulations were performed to quantify the relative contribution of deformation modes in S350, S150 and D-pass specimens. Figs. 3 (a)–(c) show the VPSC simulated stress-strain curves for S350, S150 and D-pass specimens along with corresponding experimental curves. The activity of a deformation mode refers to the sum over all grains of shear rates

1
2
3
4 contributed by that mode, weighted by grain volume fraction [36-37]. The sum of all mode
5 activities is the total activity. Thus, the relative activity of each slip/twin mode can be obtained
6 by the ratio of activity of each mode to the total activity. Since the relative activity of slip and
7 twin modes cannot be directly measured experimentally, crystal plasticity simulations were used
8 to predict the same. It is worth mentioning here that, interrupted tensile tests supplemented with
9 EBSD at different strain levels or in-situ tensile-EBSD experiments could provide valuable
10 insight to validate some features, such as the changes in dislocation density or crystal textures.
11 Figures 3 (d), (e) and (f) show the variation of relative activities of all f.c.c. and h.c.p. slip and
12 twin modes for S350, S150 and D-pass specimens, respectively. The activity curves confirm that
13 the f.c.c. slip activity decreases with progressive strain, while the h.c.p. pyramidal $\langle c+a \rangle$ slip
14 activity increases significantly with increasing strain. S350 has predominantly higher activity for
15 h.c.p. pyramidal $\langle c+a \rangle$ slip than all the other modes (Fig. 3 (d)). S150 shows the highest activity
16 for f.c.c. slip, and h.c.p. pyramidal $\langle c+a \rangle$ slip is the second most significant mode (Fig. 3 (e)).
17 Interestingly, in the D-pass specimen, f.c.c. slip and h.c.p. pyramidal $\langle c+a \rangle$ slip activities are
18 comparable (Fig. 3 (f)). Also, the activities of these two modes are relatively closer to the other
19 modes like h.c.p. basal and prismatic slip, compared to S350 or S150. For example, S150 shows
20 much higher f.c.c. slip activity than h.c.p. modes (Fig. 3 (e)), but fails to produce significant
21 work hardening. S350 features high activity of h.c.p. pyramidal $\langle c+a \rangle$ slip but f.c.c. slip activity
22 is low even at low strain (Fig. 3 (d)), because the as-FSP volume fraction of γ (f.c.c.) phase is
23 low in this condition (Fig. 1 (a) and Table 3). As a result, work hardening of S350 is better than
24 S150, but lower than the D-pass specimen. Only the D-pass specimen shows synergistic activity
25 of f.c.c. and h.c.p. deformation modes (Fig. 3 (f)). This confirms that dual-phase strain
26 partitioning is effectively achieved in the D-pass condition, thereby resulting in a sustained work
27 hardening response. In an earlier study, we sought to estimate the relative hardness of γ (f.c.c.)
28 and ϵ (h.c.p.) phases in CS-HEA from nanoindentation measurements [38]. That study showed
29 that both the phases in a dual-phase microstructure have similar hardness and modulus. While a
30 thorough independent investigation is required to truly differentiate the intrinsic deformability of
31 the two phases in this alloy, the similarity in nanoindentation response of both phases indicated
32 synergistic hardening/softening of the two phases in the microstructure, depending on thermo-
33 mechanical processing or deformation state. This further strengthens our hypothesis that the
34 synergistic hardening effect of the γ (f.c.c.) and ϵ (h.c.p.) phases is the key to sustained work
35 hardening response in CS-HEA.
36
37
38
39
40
41
42
43
44
45
46
47
48
49
50
51
52
53
54
55
56
57
58
59
60
61
62
63
64
65

1
2
3
4
5
6
7
8
9
10
11
12
13
14
15
16
17
18
19
20
21
22
23
24
25
26
27
28
29
30
31
32
33
34
35
36
37
38
39
40
41
42
43
44
45
46
47
48
49
50
51
52
53
54
55
56
57
58
59
60
61
62
63
64
65

Figure 3 (g) displays the average active systems per grain (AVACS) as a function of strain for the f.c.c. and h.c.p. phases in all three specimens. The f.c.c. phase in all three specimens shows an initial increase in AVACS followed by saturation of AVACS at higher strain. The initial increase in AVACS is attributed to γ (f.c.c.) twinning, while at higher strain, twinning activity saturates and hence, there is saturation in AVACS [39]. On the other hand, initially the h.c.p. phase decreases in AVACS after which it increases with increasing strain. Since ϵ (h.c.p.) twinning and pyramidal $\langle c+a \rangle$ slip are operative at higher strain to accommodate strain according to von Mises criterion, AVACS increases for ϵ (h.c.p.) phase at high strain. The key observation here is that AVACS increases most steeply for the S350 condition in the case of f.c.c. phase and for the S150 condition in the case of h.c.p. phase. In other words, the less dominant phase in each case undergoes rapid increase in AVACS. This is because the strain in the less dominant phase is mostly determined or imposed by the majoritarian phase to fulfill compatibility, therefore requiring higher AVACS consistent with a Taylor-like behavior. This also confirms that the metastability based alloy design induced phase evolution can alter the individual deformation responses of the two phases and the deformability of the phases is not just dependent on crystal structure.

Figure 3 (h) shows the f.c.c. and h.c.p. twin volume fractions as a function of strain for S350, S150 and D-pass conditions. D-pass specimen has the highest ϵ (h.c.p.) twin fraction, while S350 specimen also exhibits γ (f.c.c.) and ϵ (h.c.p.) twinning. Therefore, the twin fraction evolution from VPSC confirms the contribution of twinning to work hardening response (Fig. 1 (c)). The good work hardening capability of S350 is due to twinning-induced increase in strain hardening. The highest work hardening capability of D-pass specimen is attributed to the combination of TRIP and ϵ (h.c.p.) twinning. The VPSC simulations confirm that D-pass condition has the highest propensity of ϵ (h.c.p.) twinning. In line with this, stacking fault energy (SFE) is an important factor that influences the ease of twinning. In the present case, we are comparing three different microstructural states of the same alloy (CS-HEA). The SFE of our CS-HEA alloy was determined to be $\sim 6.31 \text{ mJ/m}^2$ using in-situ neutron diffraction in another study by Frank et al. [40]. This level of SFE is designed to favor ϵ -martensite transformation, while the typical SFE range for twinning is slightly higher than that of transformation. We can predict that there was some variation in the SFE between the S350, D-pass and S150 conditions of CS-HEA due to the microstructural diversity. As a result, the phase fractions in as-FSP state and the amount of γ (f.c.c.) $\rightarrow \epsilon$ (h.c.p.) transformation occurring upon tensile deformation are

different. Similarly, the ease of twinning was also different for the three different specimen conditions.

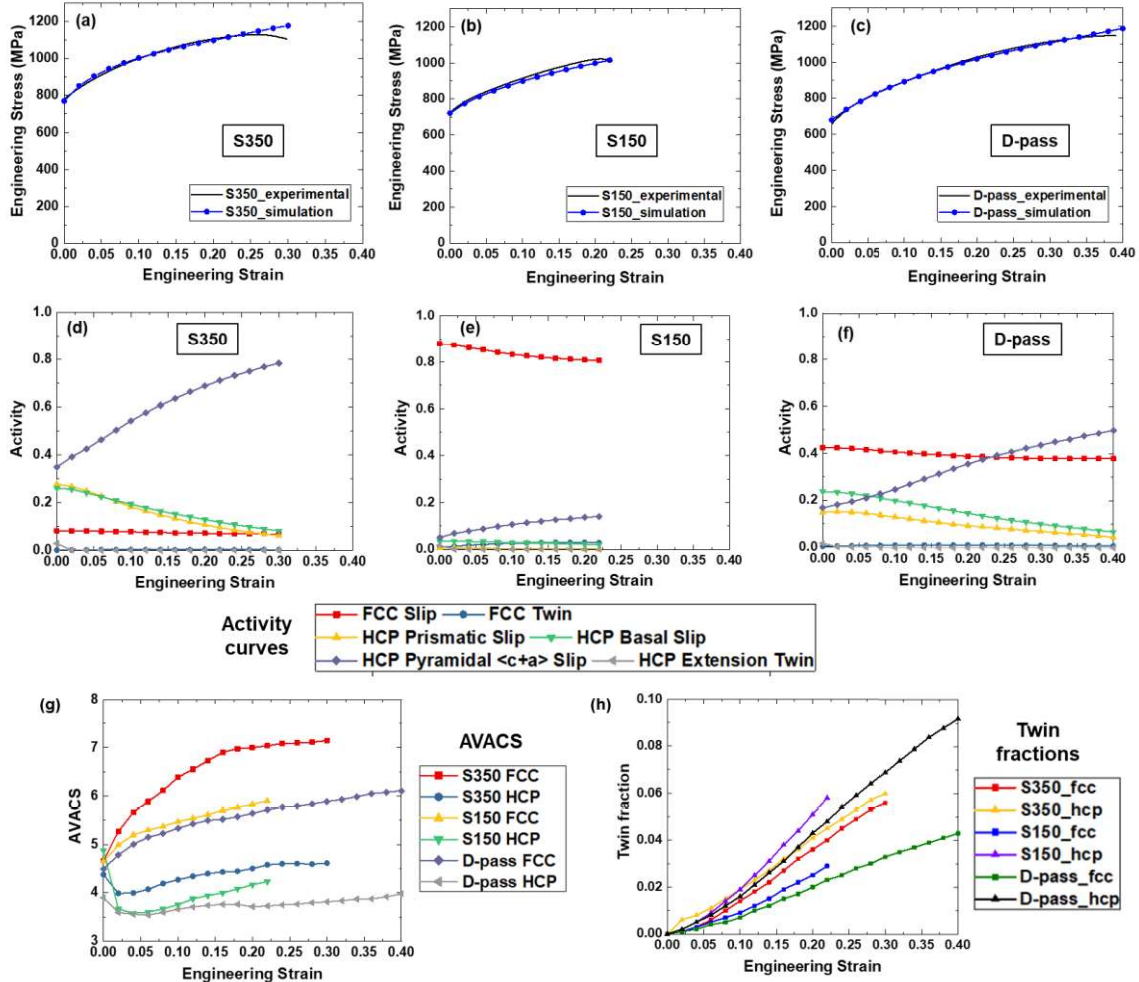


Fig. 3. VPSC simulation results. Simulated stress-strain curves in comparison with experimental curves for (a) S350 (b) S150 (c) D-pass conditions. Corresponding activity of all deformation modes as a function of strain for (d) S350 (e) S150 (f) D-pass conditions. Evolution of (g) average active slip systems (AVACS) and (h) twin volume fractions with strain for f.c.c. and h.c.p. phases in all the three conditions.

4.3. Non-uniform ductility and fracture mechanisms

Despite large uniform elongation, the CS-HEA specimens have very little non-uniform ductility (post-necking). Figure 1 (b) confirms very small non-uniform ductility region in S350 and S150 specimens, while the D-pass condition contains no non-uniform ductility at all. While uniform elongation depends on work hardening behavior, non-uniform ductility corresponds to

1
2
3
4 the growth of voids and fracture mechanisms. Therefore, the failure mechanisms of these CS-
5 HEA specimens were investigated separately by fractography and X-ray microscopy.
6

7
8 Figure 4 shows the fractography of S350, D-pass and S150 specimens of CS-HEA. S350
9 specimen exhibits mixed mode failure, wherein ductile regions are interspersed with brittle
10 faceted regions throughout the fracture surface (Fig. 4 (a2)). While Fig. 4 (a1) shows a higher
11 magnification image of a ductile region, Fig. 4 (a3) displays a brittle faceted region. The ductile
12 regions contain characteristic dimples, with voids within the dimples. The typical size of
13 voids/dimples is of the order of $1.2 \pm 1.0 \mu\text{m}$. Unlike mixed mode fracture in S350 specimen,
14 both D-pass and S150 specimens show only ductile failure features. The fracture surface of D-
15 pass specimen consists of coarse dimpled region and fine dimpled region demarcated clearly by
16 the surface along which the two halves of the tensile specimen separated (Fig. 4 (b2)). Fine
17 voids/cavities are observed within both the regions containing fine dimples (Fig. 4 (b1)) as well
18 as the coarse dimpled region (Fig. 4 (b3)). S150 specimen is characterized by formation of large
19 cavities within the surface consisting of dimples/voids (Figs. 4 (c1-c3)). This indicates a higher
20 propensity for cavity-driven failure. The average size of dimples/voids is $4.4 \pm 2.7 \mu\text{m}$, while the
21 characteristic elongated (near elliptical) cavities are $9.1 \pm 2.6 \mu\text{m}$ long and $3.7 \pm 1.2 \mu\text{m}$ wide.
22
23
24
25
26
27
28
29
30
31
32
33
34
35
36
37
38
39
40
41
42
43
44
45
46
47
48
49
50
51
52
53
54
55
56
57
58
59
60
61
62
63
64
65

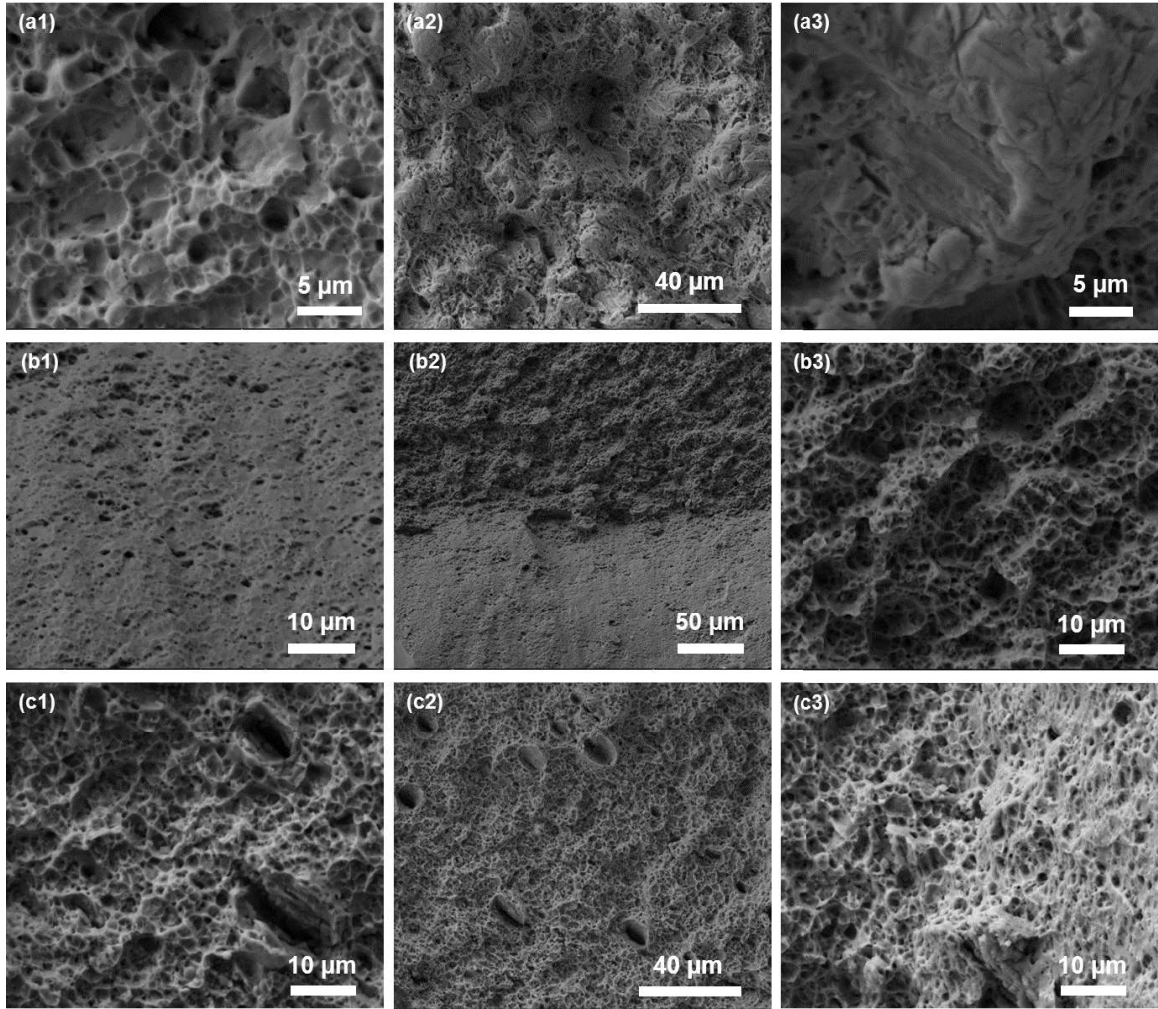
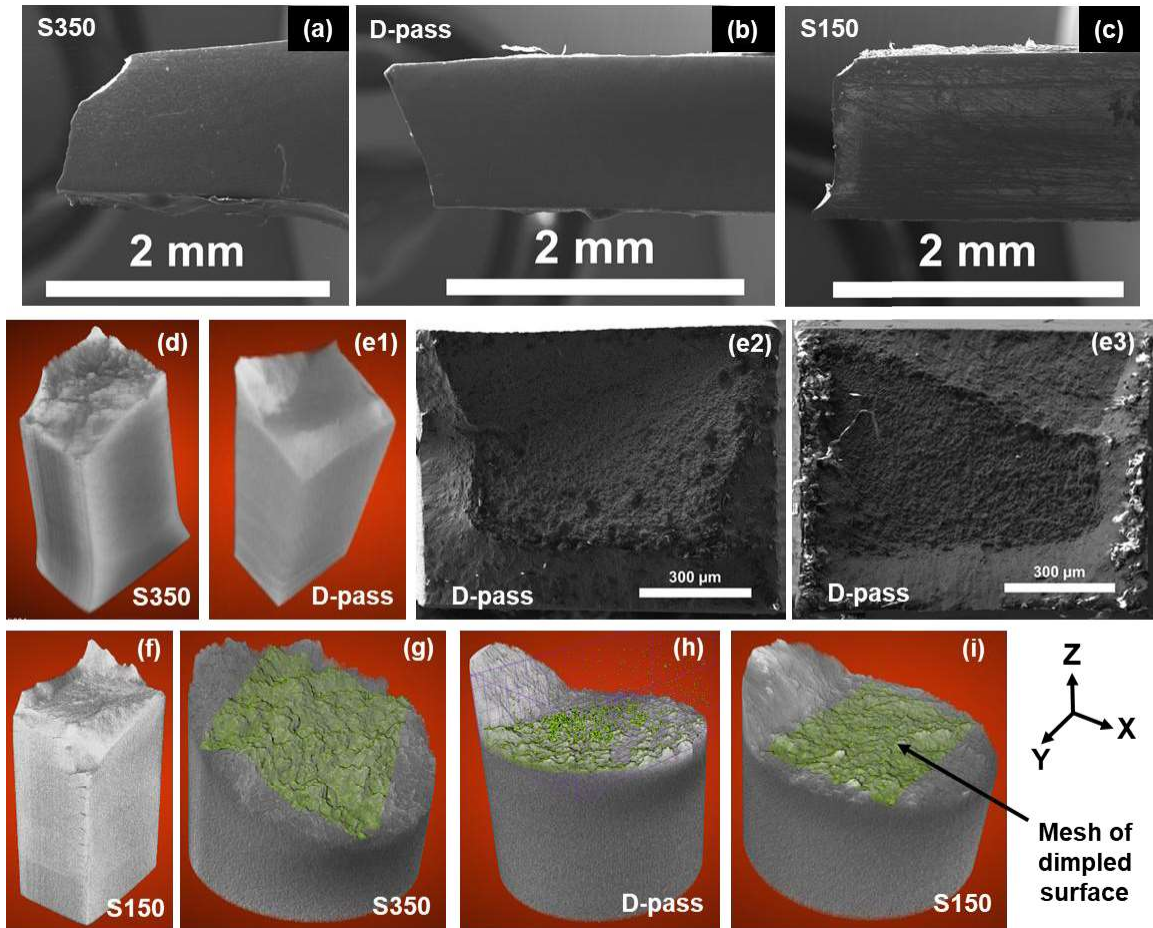


Fig.4. Fractography of CS-HEA tensile specimens, (a1-a3) S350 condition, (b1-b3) D-pass condition, and (c1-c3) S150 condition.

Figures 5 (a)–(c) are SEM images of the fractured tensile specimens of S350, D-pass and S150 conditions of CS-HEA. Distinct necking is not observed in these specimens due to the absence of significant non-uniform ductility. Figures 5 (d), (e1) and (f) are low magnification XRM images of the failed tensile specimens. S350 specimen has a dimpled fracture surface interspersed with faceted regions (Fig. 5 (d)), similar to that observed from SEM fractography. The distinct separation of the two tensile halves of D-pass specimen is indicated clearly by the XRM image in Fig. 5 (e1). Low magnification SEM fractography of both halves (Figs. 5 (e2)–(e3)) also indicates that the initiation of necking led to immediate failure in the D-pass specimen, thus creating a distinct separation interface between the two halves. Therefore, clearly, although the D-pass specimen showed highest uniform ductility due to sustained work hardening, the

1
2
3
4 sudden failure at post-necking was due to the inability to accommodate non-uniform strain.
5
6 Figure 5 (f) confirms that some cracks along the gage length are observed in the S150 specimen.
7

8 Higher magnification XRM images (Figs. 5 (g)–(i)) reveal the dimpled rupture
9 characteristics of the fracture surface. The inclined surface of S350 specimen with bigger
10 dimples suggests that the separation of the two tensile halves occurred along the surface profile
11 of the dimpled surface. In comparison, D-pass and S150 specimens show relatively flatter
12 surfaces with smaller dimples. The dimpled fracture surfaces of each specimen were extracted
13 as a mesh (green surfaces in Figs. 5 (g)–(i)) to quantify the dimple characteristics of each specimen.
14 The quantitative dimple characteristics plotted for the three specimen conditions appear in Fig. 6
15 (a). Dimples with height of the order of 20–30 μm are observed in S350 specimen, while D-pass
16 and S150 specimens have smaller dimples typically of the height of 5–10 μm . On the other hand,
17 D-pass specimen shows the highest dimple density ($\sim 107824 / \text{mm}^2$); and corresponding to the
18 highest dimple frequency, the average area covered by each dimple is lower ($\sim 9.3 \mu\text{m}^2$) than
19 S350 and S150 specimens.
20
21
22
23
24
25
26
27
28
29



1
2
3
4 **Fig. 5.** (a), (b), (c) SEM images of fractured tensile specimens, (d), (e1), (f) low magnification
5 XRM images, (e2) and (e3) SEM images of fracture surface of both halves of D-pass
6 tensile specimen, and (g), (h), (i) higher magnification XRM images with superimposed
7 mesh extracted for dimple analysis (CS-HEA specimen conditions labeled on each
8 image).
9

10
11
12 Vertical 2D slices obtained from XRM were used to observe the void characteristics beneath
13 the fracture surface. Some representative slices for each specimen condition are displayed in
14 Figs. 6 (b)–(d), while the void area fraction obtained from these slices is plotted in Fig. 6 (a). The
15 S350 specimen shows void formation beneath the fracture surface (Fig. 6 (b1)–(b2)). Such voids
16 as observed in several 2D slices confirm the occurrence of void nucleation and some void growth
17 during the ductile fracture process. In contrast, only one significantly large void was observed
18 beneath the fracture surface in the D-pass specimen (slice no. 220 in Fig. 6 (c2) out of 472
19 slices). Moreover, the fracture surface of this specimen also showed much finer voids without
20 void growth/coalescence. Therefore, void growth was clearly inhibited in the D-pass specimen,
21 consistent with the total absence of any non-uniform ductility and immediate failure after
22 initiation of necking. XRM 2D slices of S150 specimen (Fig. 6 (d1)–(d2)) displaying several
23 elongated cavities even beneath the fracture surface confirm the cavity-driven failure propensity
24 of this specimen. Overall, S350 specimen showed highest void area fraction (~2%), while D-pass
25 specimen showed lowest void area fraction (Fig. 6 (a)). Correlating void formation with starting
26 microstructure, we can conclude that the D-pass specimen with ϵ -dominant dual-phase
27 microstructure nucleates fine voids without scope for void growth; the S350 specimen with
28 almost single-phase ϵ (h.c.p.) phase shows void growth, while large cavities are formed in the
29 S150 specimen with γ -dominant dual-phase microstructure.
30
31
32
33
34
35
36
37
38
39
40
41
42

43 With regard to mechanisms driving the nucleation of voids, ductile rupture initiation by void
44 nucleation at inclusions or precipitates and second-phase particles is well known [13-14]. Noell
45 et al. discussed a mechanism of nucleation of voids in pure Ta by vacancy condensation at
46 deformation-induced boundaries such as cell block boundaries and mentioned that this
47 mechanism is not restricted to pure metals, but is also possible at microstructural features in two-
48 phase materials [41]. They also observed that some incipient subsurface voids nucleated by this
49 mechanism. Therefore, the possible void nucleation sites are the phase interfaces, grain
50 boundaries or deformation-induced boundaries such as cell block boundaries, triple junctions or
51 twin intersections [41].
52
53
54
55
56
57

58 The fracture behavior study completes the analysis of the overall tensile response of S350,
59 S150 and D-pass specimens of CS-HEA. D-pass specimen has the best uniform elongation due
60
61
62
63
64
65

1
2
3
4 to sustained work hardening by TRIP/twin effects. However, failure initiates soon after necking
5 without any non-uniform ductility. The failure occurs by ductile fracture characterized by high
6 dimple density but with limited scope for void growth. The absence of void growth explains the
7 total absence of non-uniform ductility. In contrast, S150 specimen has inferior work hardening
8 response because high TRIP kinetics inhibits the work hardening capability due to TRIP effects.
9 Also, S150 has a high propensity for cavity-driven failure. This is also attributed to significant
10 amount of γ (f.c.c.) to ε (h.c.p.) transformation with high TRIP kinetics. Higher frequency of γ/ε
11 interfaces result in more cavity nucleation sites and large cavities are formed at sites where fast
12 TRIP kinetics does not allow sufficient time to accommodate the strain mismatch between the
13 phases. As a result, the overall tensile response of S150 condition is inferior compared to S350
14 and D-pass. The reasonably good twinning-induced work hardening of the S350 specimen
15 accounts for higher uniform elongation than S150. However, mixed mode failure occurs
16 characterized by traditional cleavage brittle fracture regions as well as ductile regions with large
17 dimples. The dominance of brittle cleavage fracture regions limits the non-uniform ductility
18 although this specimen manifests some capability for accommodating non-uniform strain
19 characterized by void growth. Thus, the overall tensile response of S350 is better than S150 but
20 inferior to D-pass condition.
21
22

23
24
25
26
27
28
29
30
31
32
33 In summary, the present study revealed that the D-pass specimen of CS-HEA exhibited the
34 best strength-ductility combination due to sustained work hardening based on the synergistic
35 effect of f.c.c. and h.c.p. deformation. From a materials design point of view, the study provides
36 the following generic insight. For sustained work hardening by synergistic deformation, the
37 microstructure must be tailored to obtain a dual-phase nanocrystalline microstructure where the
38 usually harder phase between the two is the dominant phase, yet there is a significant fraction of
39 the intrinsically softer phase. This microstructural variant can be achieved by tuning the alloy
40 chemistry as well as thermo-mechanical processing. When the fractions of both phases are
41 comparable (not near single-phase before tensile deformation), the dual-phase strain partitioning
42 and strain compatibility requirements enable the simultaneous work hardening of both phases.
43 Although one phase is supposed to be intrinsically softer than the other, the hardness/modulus
44 and work hardenability/deformability of the phases in such a microstructure are more
45 compatible. Also, the mechanism of transformation induced plasticity due to deformation-
46 induced phase transformation and increase in work hardening induced by multiple deformation
47 twinning and slip mechanisms are integral to obtain such sustained work hardening response.
48 Again, this is to be achieved by combining alloy design with thermo-mechanical processing;
49
50
51
52
53
54
55
56
57
58
59
60
61
62
63
64
65

1
2
3
4 wherein, alloy design is used to modulate the stacking fault energy to favor transformation and
5 subsequent twinning, while the constituent phases must deform by multiple mechanisms whose
6 hardening propensity could be influenced by prior thermo-mechanical processing. At the same
7 time, the transformation kinetics must allow sufficient time to accommodate the strain mismatch
8 between the phases; otherwise the propensity to nucleate cavities would increase. For the same
9 reason, the transformation product phase must be the dominant phase of the dual-phase
10 microstructure and not the other way round. If the transformation parent phase fraction is higher
11 in the initial microstructure (before tensile deformation), that would increase the frequency of
12 phase interfaces that would act as potential cavity nucleation sites during tensile deformation
13 when the transformation kinetics is too fast to allow the accommodation of the strain mismatch
14 between the phases; and significant cavity nucleation could limit the ductility.
15
16
17
18
19
20
21
22
23
24
25
26
27
28
29
30
31
32
33
34
35
36
37
38
39
40
41
42
43
44
45
46
47
48
49
50
51
52
53
54
55
56
57
58
59
60
61
62
63
64
65

1
2
3
4
5
6
7
8
9
10
11
12
13
14
15
16
17
18
19
20
21
22
23
24
25
26
27
28
29
30
31
32
33
34
35
36
37
38
39
40
41
42
43
44
45
46
47
48
49
50
51
52
53
54
55
56
57
58
59
60
61
62
63
64
65

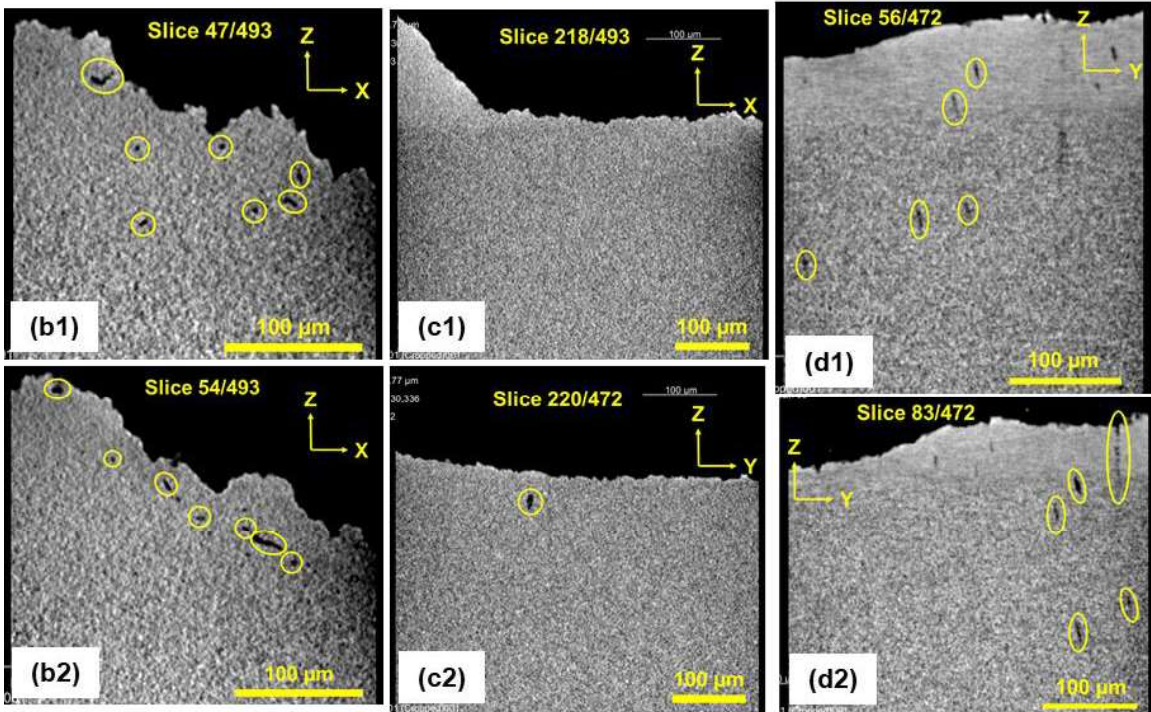
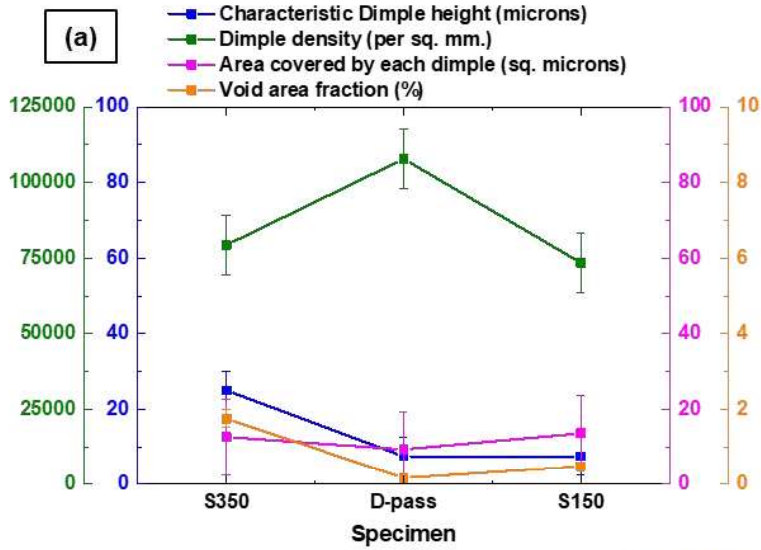


Fig. 6. (a) Dimple and void analysis from XRM of fractured tensile specimens. Representative XRM 2D slices showing voids/cavities for (b1)–(b2) S350 specimen, (c1)–(c2) D-pass specimen, and (d1)–(d2) S150 specimen of CS-HEA.

5. Discussion

5.1. Orientation dependence of resolved shear stress

The results in Section 4.1 proved that the amount of transformation/twinning induced work hardening significantly contributes to the strength-ductility response of CS-HEA. Therefore, an important question that follows is what causes a γ (f.c.c.) grain to transform to ϵ (h.c.p.) during

1
2
3
4 deformation. This is fundamentally based on the fact that in f.c.c. metals, perfect dislocations
5 dissociate into Shockley partials leaving a stacking fault (SF) between them [42]. The effect of
6 applied stress on the separation distance between partials is as strong as the effect of SFE [42].
7 Deformed microstructures of austenitic stainless steels often show SF ribbons with 1 μm
8 separation between the two partials [42].
9

10
11 Polatidis et al. discussed that when the leading partial dislocation (LPD) has higher Schmid
12 factor (m) than the trailing partial dislocation (TPD), the separation between the partials
13 increases due to applied stress, resulting in local formation of ϵ (h.c.p.) martensite phase [43].
14 Additionally, resolved shear stress (RSS) or Schmid factor depends on γ (f.c.c.) grain orientation
15 with respect to the applied stress direction. Hence, the first step to calculate RSS on LPD and
16 TPD is to map the orientation dependence of ‘ m ’.
17

18
19 Figure 7 (a) shows the orientations of various f.c.c. crystallographic directions on the
20 stereographic inverse pole figure (IPF) triangle. Schmid factors were calculated for the $\{111\} <$
21 $1\bar{1}0 >$ slip system for various grain orientations whose tensile axes are along the directions in
22 Fig. 7 (a). Figs. 7 (b-i) exhibit the tensile axis IPFs mapping Schmid factor distribution for
23 different variants of the slip system $\{111\} < 1\bar{1}0 >$ (e.g. $(111)[1\bar{1}0]$, $(\bar{1}10)[101]$ etc.). Note
24 that, ‘ m ’ distributions of 8 variants are mapped in Figs. 7 (b-i). The remaining 4
25 variants, $(111)[01\bar{1}]$, $(111)[10\bar{1}]$, $(\bar{1}11)[01\bar{1}]$ and $(1\bar{1}1)[10\bar{1}]$, have negative/zero ‘ m ’ values
26 for all orientations contained in Fig. 7 (a). The highest Schmid factor is obtained for $[102]$ tensile
27 axis for the $(1\bar{1}1)[011]$ slip system variant (outlined by black rectangle in Fig. 7 (h)).
28 Interestingly, γ (f.c.c.) grains in the D-pass specimen of CS-HEA (that showed the highest TRIP
29 induced work hardening (Fig. 1 (c)) exhibit a tensile axis IPF with maximum intensity at $[102]$,
30 as depicted by Figs. 7 (j) and (k).
31

32
33 The corresponding glide shear strain distribution was also obtained as a function of IPF
34 orientation of tensile axis. Fig. 7 (l) maps a shear strain distribution on IPF that was calculated
35 from Eq. (6) using the assumption that the axial strain is same for all the orientations.
36

$$\varepsilon = \gamma m \quad (6)$$

37
38 where ε is the axial strain, γ is the shear strain and m is the Schmid factor. Thus, the contours on
39 Fig. 7 (j) are an exact replica of the ‘ m ’ distribution IPF Fig. 7 (h), except that the relative
40 intensities are inversely related. Thus, $[102]$ orientation shows lower strain level than the other
41 orientations, because ‘ m ’ (and hence, RSS) was highest for $[102]$ in Fig. 7 (h). In reality, the
42 axial strain is also different for the different orientations. Therefore, a more appropriate way to
43

1
2
3
4 calculate shear strain dependence of crystallographic orientation is from Eq. (7) [25], using a
5 certain value of global strain,
6

$$\gamma = \{1/(\sin \chi_0)\}[\{(L_i/L_0)^2 - \sin^2 \lambda_0\}^{1/2} - \cos \lambda_0] \quad (7)$$

7
8 where, χ_0 and λ_0 are the angles specifying the orientations of the slip plane and slip direction
9 with respect to the tensile (loading) axis and L_i/L_0 represents the macroscopic engineering strain.
10 The glide shear strain distribution thus obtained for $(1\bar{1}1)[011]$ slip is plotted on the IPF triangle
11 in Fig. 7 (m). The corresponding axial strain distribution calculated from the shear strain in Fig.7
12 (m) is plotted in Fig. 7 (n). Figs. 7 (m-n) indicate higher strain concentration on the ‘hard
13 orientations’ (e.g. $[112]$ or $[111]$) than ‘soft orientations’ that exhibit high Schmid factor in Fig. 7
14 (h) (e.g. $[102]$). In short, the quantitative analysis of IPF orientation dependence of ‘m’ reveals
15 that the RSS is highest for $\{111\} \langle 1\bar{1}0 \rangle$ slip when the grain is oriented such that its $\langle 012 \rangle$
16 direction is parallel to the tensile axis. Next, we obtained the RSS on LPD and TPD for the
17 various $\langle 012 \rangle$ directions.
18
19
20
21
22
23
24
25
26
27
28
29
30
31
32
33
34
35
36
37
38
39
40
41
42
43
44
45
46
47
48
49
50
51
52
53
54
55
56
57
58
59
60
61
62
63
64
65

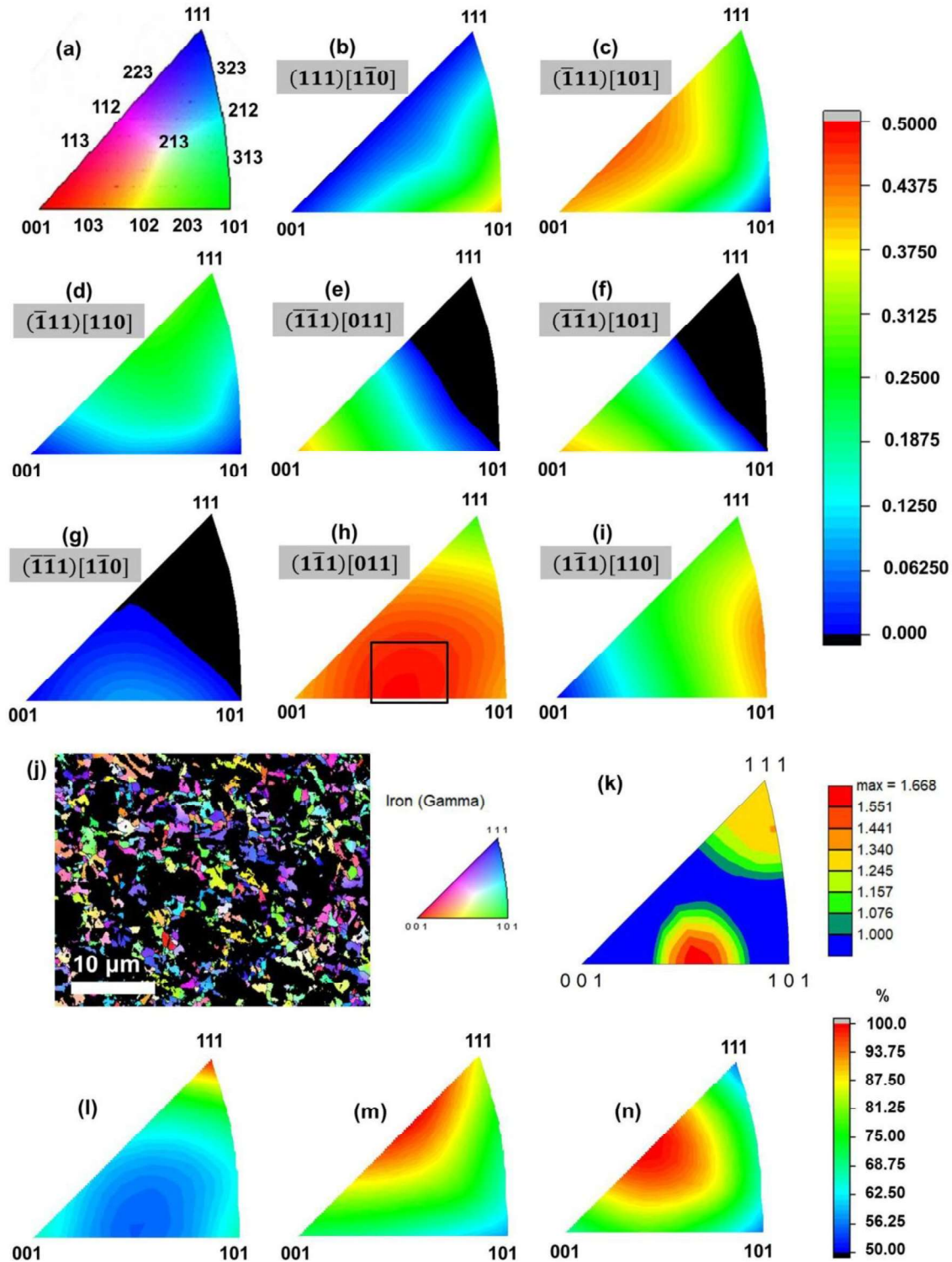


Fig. 7. (a) Tensile axis IPF orientations (b-i) Theoretical Schmid factor distributions on IPFs for different variants of $\{111\} \langle 110 \rangle$ slip system (j) Experimental tensile axis IPF map orientation of γ (f.c.c.) grains in D-pass specimen of CS-HEA and (k) corresponding tensile axis IPF (l-n) Theoretical glide shear strain and axial strain distributions on IPFs. Note that ‘m’

distributions of 8 variants are mapped in (b-i), while the remaining 4 variants $(111)[01\bar{1}]$, $(111)[10\bar{1}]$, $(\bar{1}11)[01\bar{1}]$ and $(\bar{1}11)[10\bar{1}]$ have negative/zero ‘m’ values.

5.2. Resolved shear stress on partial dislocations and probability of martensitic transformation

The tensile axis orientations of $\langle 012 \rangle$ family are superimposed on a 001 stereographic projection of f.c.c. crystal structure in Fig. 8 (a). Note that Fig. 8 (a) is not a pole figure in the true sense of the word. However, since the f.c.c. crystal structure consists of three orthogonal axes that are equal in magnitude, the normal to a plane (pole of the plane) lies along the direction with the same Miller indices. For example, the pole of the (111) plane is the [111] direction. Therefore, we can conclude from Fig. 8 (a) that the orientation with the highest RSS is when the tensile axis is perpendicular to one of the planes of $\{012\}$ family. A pole figure representing the texture with highest RSS would look like Fig. 8 (a). Fig. 8 (b) shows the multiplicity of the tensile axis directions with highest RSS on a 3D Wulff net (since the bottom hemisphere is not revealed in Fig. 8 (a)). The RSS on LPD and TPD for $[\bar{1}02]$, $[012]$, $[0\bar{1}2]$ and $[102]$ directions were obtained as a function of the applied tensile flow stress (Figs. 8 (c-f)). Due to symmetry, the RSS on LPD/TPD for the directions in the bottom hemisphere of Fig. 8 (b) are same as the direction of opposite sense in the top hemisphere. The difference in RSS between LPD and TPD increases with applied stress for $[\bar{1}02]$, $[012]$, $[0\bar{1}2]$; only $[102]$ shows the same RSS for LPD and TPD because both have the same Schmid factor in the latter case. $[0\bar{1}2]$ shows the highest increase in the difference between RSS of LPD and RSS of TPD with increase in applied stress (Fig. 8 (e)). Hence, grains oriented with $[0\bar{1}2]$ along the tensile axis would have the highest tendency for separation of partials due to applied stress. Thus, we conclude that γ (f.c.c.) grains oriented with $[0\bar{1}2] //$ tensile axis would favor deformation induced γ (f.c.c.) \rightarrow ε (h.c.p.) transformation.

The elastic force per unit length between two parallel partial dislocations, F_{AB} , is given by [44],

$$F_{AB} = K(\alpha)/x = Gb_p^2(2 - \nu)[1 - \{2\nu \cos^2 \alpha / (2 - \nu)\}] / 8\pi x(1 - \nu) \quad (8)$$

where $K(\alpha)$ is the elastic force between the partial dislocations, x is the separation distance between the partials, G is the shear modulus, b_p is the Burgers vector of the partial dislocation, ν is the Poisson ratio and α is the angle between the Burgers vector of the total dislocation. The equilibrium separation between the partial dislocations is given by [44],

$$x_{eqbm} = K(\alpha)/\gamma \quad (9)$$

where γ is the stacking fault energy. This means that for applied stress to increase the separation of the partials, the condition specified by Eq. (9) must be broken so that the leading partial moves farther away from the trailing partial. To restore the equilibrium while the partial dislocation moves, Eq. (10) must be satisfied [44],

$$-K(\alpha)/x + \gamma + (\boldsymbol{\sigma} \cdot \mathbf{b}_p) \cdot \mathbf{n} = 0 \quad (10)$$

where $\boldsymbol{\sigma}$ is the dyadic representing the applied stress and \mathbf{n} is the unit vector normal to the slip plane. Since $(\boldsymbol{\sigma} \cdot \mathbf{b}_p) \cdot \mathbf{n} = \tau b_p$ (τ being the shear component of the applied stress on the slip plane in the direction of \mathbf{b}_p). Eq. (10) can be written as,

$$-K(\alpha)/x + \gamma + \tau b_p = 0. \quad (11)$$

Thus, we can calculate the critical value of shear component of applied stress required to increase the separation of partial dislocations from Eq. (11). This calculation was performed assuming a partial separation distance of 1 μm and using a SFE of 15 mJ/m^2 because the range of SFE for TRIP is 10-20 mJ/m^2 [45-46]. The critical value of the shear component of applied stress (τ_{crit}) to increase the partial separation was estimated as 100 MPa. When we plot τ_{crit} on the RSS on LPD/TPD graph (black dotted lines in Figs. 8 (c-f)), we get an estimate of the threshold applied tensile flow stress (σ_{thr}) at which γ (f.c.c.) to ϵ (h.c.p.) transformation can be triggered by increasing the partial separation for the different $\langle 012 \rangle$ tensile directions discussed. The applied stress corresponding to the intersection of τ_{crit} with the RSS on LPD gives σ_{thr} . The values of σ_{thr} obtained for $[\bar{1}02]$, $[012]$ and $[0\bar{1}2]$ directions are 1312 MPa, 1313 MPa and 731 MPa, respectively (Figs. 8 (c), (d) and (e), respectively). The experimental engineering stress-strain curves for S350, S150 and D-pass specimens were shown in Fig. 1 (b) and the corresponding experimental flow stresses were plotted in Figs. 2 (a), (b) and (c) for S350, S150 and D-pass specimens, respectively. Since the σ_{thr} values obtained from Figs. 8 (c-e) correspond to flow stresses, they should be compared with the experimental flow stresses in Figs. 2 (a-c). The experimental true yield stresses for S350, S150 and D-pass specimens are 777 MPa, 723 MPa and 657 MPa, respectively (Figs. 2 (a), (b) and (c), respectively). This implies that transformation can be triggered in γ (f.c.c.) grains oriented with its $[0\bar{1}2]$ crystallographic direction parallel to the tensile loading axis (with $\sigma_{\text{thr}} = 731$ MPa) at stresses very near to the yield point in these specimens. Further, the engineering plastic strain corresponding to the hump in the strain hardening curve of D-pass specimen is in the range of 0.15-0.2 (Fig. 1 (c)). Taking the engineering plastic strain value of 0.175 within this range, the corresponding engineering stress is 995 MPa for D-pass specimen (Fig. 1 (b)). This corresponds to a true flow stress of 1169 MPa (Fig. 2 (c)). When applied tensile flow stress is increased from σ_{thr} of $[0\bar{1}2]$ orientation

1
2
3
4
5
6
7
8
9
10
11
12
13
14
15
16
17
18
19
20
21
22
23
24
25
26
27
28
29
30
31
32
33
34
35
36
37
38
39
40
41
42
43
44
45
46
47
48
49
50
51
52
53
54
55
56
57
58
59
60
61
62
63
64
65

(731 MPa) to 1169 MPa, the difference between RSS of LPD and RSS of TPD increases from 100 to 160 MPa (Fig. 8 (e)). Thus, we have quantitatively established through this study that γ (f.c.c.) grains with $[0\bar{1}2]$ parallel to the tensile loading axis are favorable for undergoing γ (f.c.c.) to ϵ (h.c.p.) transformation and the threshold value of applied tensile flow stress for this orientation is 731 MPa.

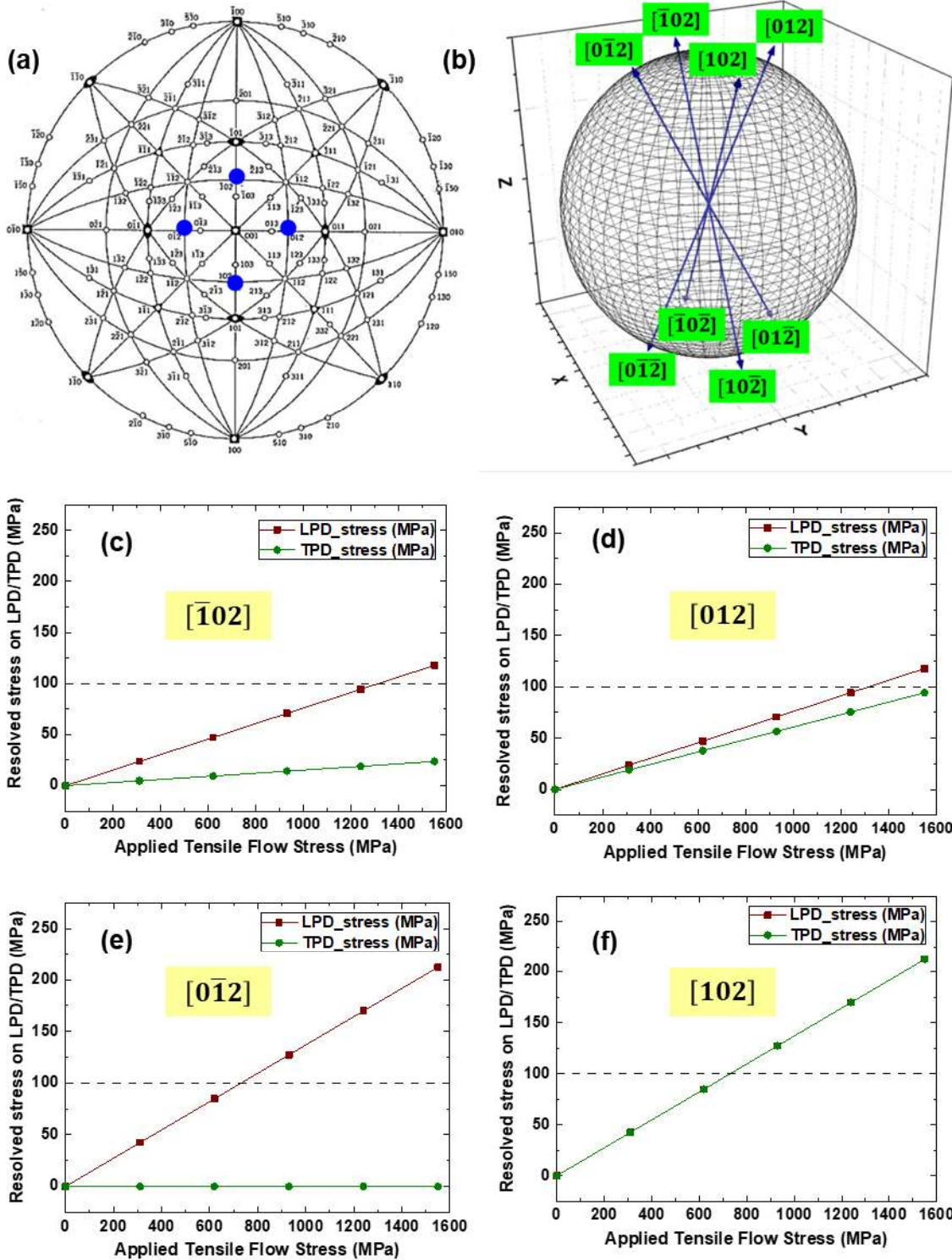


Fig. 8. (a) 001 stereographic projection of f.c.c. with superimposed tensile axis orientations with highest resolved shear stress for $(\bar{1}\bar{1}1)[011]$ slip, and (b) multiplicity of the tensile axis orientation in (a) shown on 3D reference sphere. Resolved shear stress on leading and trailing partial dislocations as a function of applied tensile flow stress for (c) $\bar{1}02$, (d) 012 , (e) $0\bar{1}2$, and (f) 102 tensile axes.

1
2
3
4
5
6 **6. Summary**

7 The following conclusions were drawn from the present study of deformation mechanisms
8 and fracture behavior of Fe₄₀Mn₂₀Co₂₀Cr₁₅Si₅ HEA (CS-HEA) processed by FSP using different
9 tool rotation rates (S350: single pass at 350 rpm; S150: single pass at 150 rpm; and D-pass:
10 consecutive overlapping passes at 350 and 150 rpm).
11

- 12 1. All three conditions (S350, S150 and D-pass) showed significant uniform elongation but
13 limited non-uniform ductility in quasi-static tensile test. Therefore, a strong microstructural
14 dependence of work hardening behavior due to the additional contribution of TRIP/twin
15 effects differentiates the strength-ductility response of these specimens. Microstructural
16 dependence of fracture initiation is less significant; nevertheless, some differences in the
17 capacity for void nucleation and growth contribute to their propensity for ductile failure after
18 necking.
19
- 20 2. Among the three conditions, D-pass specimen showed the highest additional hardening
21 contribution (~ 500 MPa at UTS) from TRIP/twin effects over and above the contributions
22 of linear Taylor dislocation hardening and geometrical hardening. The crystallographic
23 orientation dependence of resolved shear stress on leading and trailing partial dislocations
24 was quantified to reveal that theoretically, γ (f.c.c.) grains with $[0\bar{1}2]$ // tensile axis are
25 favorable for γ (f.c.c.) to ε (h.c.p.) transformation and the threshold value of applied tensile
26 flow stress for this grain orientation is 731 MPa.
27
- 28 3. Crystal plasticity simulations using VPSC model confirmed that synergistic activity of f.c.c.
29 and h.c.p. deformation modes enabled sustained work hardening by dual-phase strain
30 partitioning in the D-pass specimen, thereby accounting for highest uniform elongation in
31 this specimen.
32
33
34
35
36
37
38
39
40
41
42
43
44
45
46

47 **Acknowledgments**

48 The work was performed under the cooperative agreement of University of North Texas with the
49 U.S. Army Research Laboratory (W911NF-18-2-0067). We thank Materials Research Facility
50 and Advanced Materials and Manufacturing Processes Institute at University of North Texas for
51 access to scanning electron microscopy and X-ray microscopy facilities, respectively. We are
52 grateful to Drs. Hrishikesh Bale, Rachna Parwani and Robin White from Zeiss for training us on
53 the X-ray microscope.
54
55
56
57
58
59
60
61
62
63
64
65

References

- [1] Z. Li, K.G. Pradeep, Y. Deng, D. Raabe, C.C. Tasan, Metastable high-entropy dual-phase alloys overcome the strength-ductility trade-off, *Nature*, 534 (2016) 227-230.
- [2] Z. Li, D. Raabe, Strong and ductile non-equiatomic high-entropy alloys: Design, processing, microstructure, and mechanical properties, *JOM* 69 (2017) 2099-2106.
- [3] Z. Li, C.C. Tasan, H. Springer, B. Gault, D. Raabe, Interstitial atoms enable joint twinning and transformation induced plasticity in strong and ductile high-entropy alloys, *Sci. Reports*, 7 (2017) 40704-1–40704-7.
- [4] S.S. Nene, K. Liu, M. Frank, R.S. Mishra, R.E. Brennan, K.C. Cho, Z. Li, D. Raabe, Enhanced strength and ductility in a friction stir processing engineered dual phase high entropy alloy, *Sci. Reports*, 7 (2017) 16167-1–16167-7.
- [5] S.S. Nene, M. Frank, K. Liu, R.S. Mishra, B.A. McWilliams, K.C. Cho, Extreme high strength and work hardening ability in a metastable high entropy alloy, *Sci. Reports*, 8 (2018) 9920-1–9920-8.
- [6] S.S. Nene, M. Frank, K. Liu, S. Sinha, R.S. Mishra, B.A. McWilliams, K.C. Cho, Reversed strength-ductility relationship in microstructurally flexible high entropy alloy, *Scripta Mater.*, 154 (2018) 163-167.
- [7] S.S. Nene, S. Sinha, M. Frank, K. Liu, R.S. Mishra, B.A. McWilliams, K.C. Cho, Unexpected strength–ductility response in an annealed, metastable, high-entropy alloy, *Appl. Mater. Today*, 13 (2018) 198-206.
- [8] S. Sinha, S.S. Nene, M. Frank, K. Liu, R.S. Mishra, B.A. McWilliams, K.C. Cho, Microstructural Evolution and Deformation Behavior of Ni-Si-and Co-Si-Containing Metastable High Entropy Alloys, *Met. Mater. Trans. A*, 50 (2019) 179-190.
- [9] L. Liliensten, J-P. Couzinié, J. Bourgon, L. Perrière, G. Dirras, F. Prima, I. Guillot, Design and tensile properties of a bcc Ti-rich high-entropy alloy with transformation-induced plasticity, *Mater. Res. Lett.* 5 (2017) 110-116.
- [10] L. Zhang, H. Fu, S. Ge, Z. Zhu, H. Li, H. Zhang, A. Wang, H. Zhang, Phase transformations in body-centered cubic Nb_xHfZrTi high-entropy alloys, *Mater. Char.* 142 (2018) 443-448.
- [11] S. Wei, J. Kim, C.C. Tasan, Boundary micro-cracking in metastable Fe₄₅Mn₃₅Co₁₀Cr₁₀ high-entropy alloys, *Acta Mater.* 168 (2019) 76-86.
- [12] Z.C. Luo, M.X. Huang, Revealing the fracture mechanism of twinning-induced plasticity steels, *Steels Res. Int.* 1700433 (2018) 1-7.
- [13] G. Le Roy, J.D. Embury, G. Edwards, M.F. Ashby, A model of ductile fracture based on the nucleation and growth of voids, *Acta Metall.* 29 (1981) 1509-1522.
- [14] V. Tvergaard, A. Needleman, Analysis of the cup-cone fracture in a round tensile bar, *Acta Metall.* 32 (1984) 157-169.
- [15] A. Weck, D.S. Wilkinson, E. Maire, Observation of void nucleation, growth and coalescence in a model metal matrix composite using X-ray tomography, *Mater. Sci. Eng. A* 488 (2008) 435-445.
- [16] P.F. Thomason, Ductile fracture by the growth and coalescence of microvoids of non-uniform size and spacing, *Acta Metall.* 41 (1993) 2127-2134.
- [17] G.I. Taylor, The mechanism of plastic deformation of crystals, *Proc. Roy. Soc. A* 145 (1934) 362-404.
- [18] H. Wiedersich, Hardening mechanisms and the theory of deformation, *JOM* 16 (1964) 425-430.

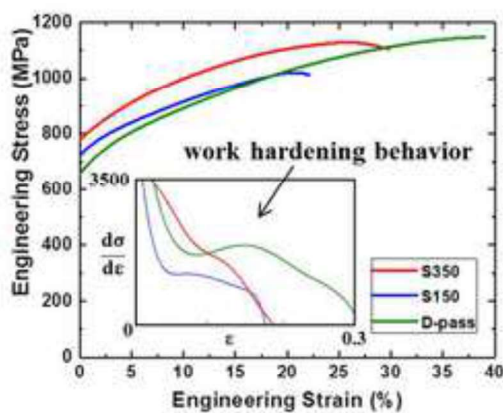
- 1
2
3
4 [19] H. Mecking, U.F. Kocks, Kinetics of flow and strain-hardening, *Acta Metall.* 29 (1981)
5 1865-1875.
6
7 [20] U.F. Kocks, H. Mecking, Physics and phenomenology of strain hardening: the FCC case,
8 *Prog. Mater. Sci.* 48 (2003) 171-273.
9
10 [21] K.M. Davoudi, J.J. Vlassak, Dislocation evolution during plastic deformation: Equations vs.
11 discrete dislocation dynamics study, *J. Appl. Phys.* 123 (2018) 085302-1–085302-8.
12
13 [22] T. Takeshita, H-R. Wenk, Plastic anisotropy and geometrical hardening in quartzites,
14 *Tectonophysics* 149 (1988) 345-361.
15
16 [23] M. Miller, P. Dawson, Influence of slip system hardening assumptions on modeling stress
17 dependence of work hardening, *J. Mech. Phys. Solids* 45 (1997) 1781-1804.
18
19 [24] F.F. Lavrentev, The type of dislocation interaction as the factor determining work
20 hardening, *Mater. Sci. Eng.* 46 (1980) 191-208.
21
22 [25] G.E. Dieter, *Mechanical Metallurgy*, Si Metric Ed. McGraw-Hill Book Company, London,
23 1988, pp. 127-130.
24
25 [26] R.A. Lebensohn, C.N. Tome, A self-consistent anisotropic approach for the simulation of
26 plastic deformation and texture development of polycrystals: Application to zirconium
27 alloys, *Acta Metall. Mater.* 41 (1993) 2611-2624.
28
29 [27] C.N. Tome, R.A. Lebensohn, *Visco-plastic self-consistent (VPSC) Version 7c Manual*,
30 2009.
31
32 [28] C. Tome, G.R. Canova, U.F. Kocks, N. Christodoulou, J.J. Jonas, The relation between
33 macroscopic and microscopic strain hardening in f.c.c. polycrystals, *Acta Metall.* 32 (1984)
34 1637-1653.
35
36 [29] S. Sinha, J.A. Szpunar, N.A.P. Kiran Kumar, N.P. Gurao, Tensile deformation of 316L
37 austenitic stainless steel using in-situ electron backscatter diffraction and crystal plasticity
38 simulations, *Mater. Sci. Eng. A* 637 (2015) 48-55.
39
40 [30] H. Wang, P.D. Wu, C.N. Tome, J. Wang, Study of lattice strains in magnesium alloy AZ31
41 based on a large strain elasto-viscoplastic self-consistent polycrystal model, *Int. J. Solids
42 Struct.* 49 (2012) 2155-2167.
43
44 [31] V.M. Miller, T.D. Berman, I.J. Beyerlein, T.M. Pollock, Prediction of magnesium alloy
45 formability: The role of texture, In: *Magnesium Technology* (Eds. A. Singh, K. Solanki,
46 M.V. Manuel, N.R. Neelameggham), Springer, Cham (2016) pp. 257-262.
47
48 [32] S. Sinha, A. Ghosh, N.P. Gurao, Effect of initial orientation on the tensile properties of
49 commercially pure titanium, *Phil. Mag.* 96 (2016) 1485-1508.
50
51 [33] A. Mangal, E.A. Holm, Applied machine learning to predict stress hotspots II: Hexagonal
52 close packed materials, *Int. J. Plast.* 114 (2019) 1-14.
53
54 [34] X. Li, D. L. Irving, L. Vitos, First-principles investigation of the micromechanical properties
55 of fcc-hcp polymorphic high-entropy alloys, *Sci. Reports.* 8 (2018) 11196-1–11196-8.
56
57 [35] P. Yu, L. Zhang, H. Cheng, H. Tang, J. Fan, P.K. Liaw, G. Li, R. Liu, Formation, reverse
58 transformation, and properties of ϵ -martensite phase in the CoCrFeMnNi high-entropy alloy
59 under high-pressure, *J. Alloys Compds.* 779 (2019) 1-6.
60
61 [36] K.E.K. Amouzou, T. Richeton, A. Roth, M.A. Lebyodkin, T.A. Lebedkina,
62 Micromechanical modeling of hardening mechanisms in commercially pure α -titanium in
63 tensile condition, *Int. J. Plast.* 80 (2016) 222-240.
64
65 [37] S. Sinha, N. P. Gurao, In-plane anisotropy in mechanical behavior and microstructural
evolution of commercially pure titanium in tensile and cyclic loading, *Met. Mater. Trans. A*
48A (2017) 5813-5832.

- 1
2
3
4 [38] S. Sinha, R.A. Mirshams, T. Wang, S.S. Nene, M. Frank, K. Liu, R.S. Mishra,
5 Nanoindentation behavior of high entropy alloys with transformation-induced plasticity, *Sci.*
6 *Reports* 9 (2019) 6639-1–6639-11.
7
8 [39] N.P. Gurao, P. Kumar, B. Bhattacharya, A. Haldar, S. Suwas, Evolution of crystallographic
9 texture and microstructure during cold rolling of twinning-induced plasticity (TWIP) steel:
10 Experiments and simulations, *Met. Mater. Trans. A* 43A (2012) 5193-5201.
11
12 [40] M. Frank, Y. Chen, S.S. Nene, S. Sinha, K. Liu, K. An, R.S. Mishra, Investigating the
13 deformation mechanisms of a highly metastable high entropy alloy using in-situ neutron
14 diffraction, Manuscript under revision, *Mater. Today Comm.* (2019).
15
16 [41] P. Noell, J. Carroll, K. Hattar, B. Clark, B. Boyce, Do voids nucleate at grain boundaries
17 during ductile rupture?, *Acta Mater.* 137 (2017) 103-114.
18
19 [42] T.S. Byun, On the stress dependence of partial dislocation separation and deformation
20 microstructure in austenitic stainless steels, *Acta Mater.* 51 (2003) 3063-3071.
21
22 [43] E. Polatidis, W.-N. Hsu, M. Šmíd, T. Panzner, S. Chakrabarty, P. Pant, H. Van
23 Swygenhoven, Suppressed martensitic transformation under biaxial loading in low stacking
24 fault energy metastable austenitic steels, *Scripta Mater.* 147 (2018) 27-32.
25
26 [44] P.B. Hirsch, A. Kelly, Stacking-fault strengthening, *Phil. Mag.* 12 (1965) 881-900.
27
28 [45] S. Martin, S. Wolf, U. Martin, L. Krüger, D. Rafaja, Deformation mechanisms in austenitic
29 TRIP/TWIP steel as a function of temperature, *Met. Mater. Trans. A* 47A (2016) 49-58.
30
31 [46] E.I. Galindo-Nava, P.E.J. Rivera-Díaz-del-Castillo, Understanding martensite and twin
32 formation in austenitic steels: A model describing TRIP and TWIP effects, *Acta Mater.* 128
33 (2017) 120-134.
34
35
36
37
38
39
40
41
42
43
44
45
46
47
48
49
50
51
52
53
54
55
56
57
58
59
60
61
62
63
64
65

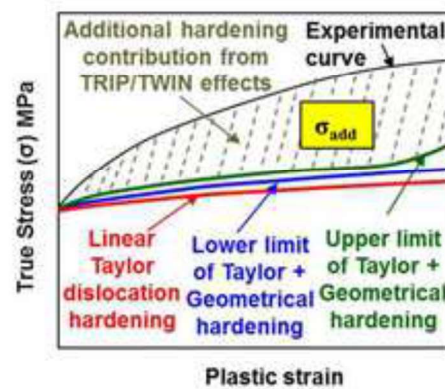
*Graphical Abstract



$Fe_{40}Mn_{20}Co_{20}Cr_{15}Si_5$ (CS-HEA)
As-cast → As-FSP
Phase evolution



D-pass specimen shows the highest uniform elongation and sustained work hardening behavior



$\sigma_{add} = 500$ MPa for D-pass
300 MPa for S350
200 MPa for S150